Journal of Materials Chemistry A

Accepted Manuscript

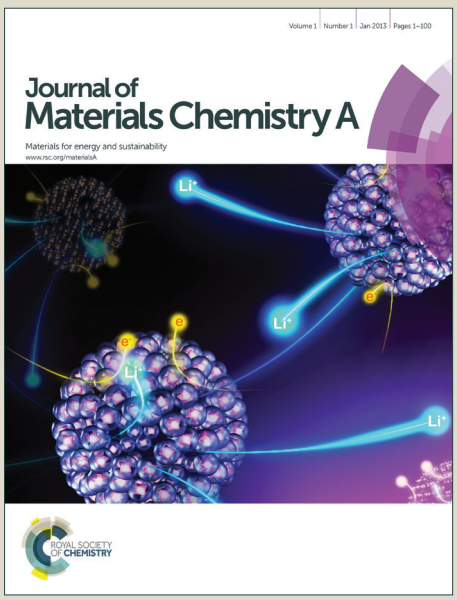

ROYAL SOCIETY OF CHEMISTRY

www.rsc.org/materialsA

Journal of Materials Chemistry

Journal of Materials Chemistry A

Dynamic Article Links ►

Cite this: DOI: 10.1039/c0xx00000x

www.rsc.org/xxxxxx

Paper

MnO_2 Nanostructures with Three-dimensional (3D) Morphology Replicated from Diatoms for High-Performance Supercapacitors

Fei Li[a], Yuan Xing[a], Ming Huang[a,b], Kai Lin Li[a], Ting Ting Yu[a], Yu Xin Zhang[a,c]*, Dusan Losic[d]*

Received (in XXX, XXX) Xth XXXXXXXXX 20XX, Accepted Xth XXXXXXXXX 20XX

DOI: 10.1039/b000000x

Herein, we demonstrate the synthesis of size- and shape-controlled MnO_2 nanostructures by replica molding from diatom silica structures for high-performance supercapacitors. Three types of hierarchical hollow MnO_2 patterns with different three-dimensional (3D) structure, shapes and large surface area were successfully prepared from three diatom species by a template-assisted hydrothermal process. The extraordinary precision and nano-scale resolution of 3D replications of complex biologal architecture from diatoms to artificial MnO_2 structures is confirmed. Detailed electrochemical measurements reveal that melosira-type MnO_2 pattern exhibits not only high specific capacitance of 371.2 F g^{-1} at a scan rate of 0.5 A g^{-1}, but also relatively good cycle stability (93.1% capacitance retention after 2000 cycles at a scan rate of 5 A g^{-1}), demonstrating a promising application as supercapacitor electrode materials.

Introduction

Electrochemical supercapacitors based on manganese dioxides (MnO_2) have attracted intensive interest because of low cost, high activity/stability in alkaline/neutral media, environmental compatibility, and abundant availability[1-3]. Up to now, manganese oxides with various structures and morphologies such as nanosheets[4], hollow nanospheres[5], nanoflowers[6], nanowires/nanorods[7, 8], thin films[9], and nanotubes[10] have been fabricated via electrochemical and chemical routes, and their electrochemical properties have been investigated. These studies indicate that designing of MnO_2-based nanomaterials with complex three dimensional (3D) structures is critical for these applications due to their significantly improved capacitance and cyclic stability[11-14]. However, fabrication of MnO_2-based nanomaterials with well-defined and precisely controlled 3D morphologies with combined micro-to-nano scale features remains a significant challenge. Therefore there is a strong demand for inexpensive methods for fabrication of complex 3D structures with high degree of precision and reproducibility.

This synthetic problem is successfully solved in nature showing many examples of living organisms with this micro-to-nano structures with multifunctional properties. Therefore it is not surprising that biological materials and processes are recognized as a new source of inspiration for the design and fabrication of nano-structured materials with complex morphology. The amorphous silica exoskeletons (frustules) of the single-celled algae called diatoms with extraordinary 3D structure, are the most outstanding examples provided by nature through unique self-assembly process, because of its numerous fine microscopic pores, large specific surface area, and high absorption capacity[15-18]. During the last two centuries, the importance of diatoms in the field of microtechnology and nanotechnology has become increasingly evident. The unique properties of diatom silica, supplied from inexpensive sources such as diatom cultures or diatom (Diatomaceous Earth, DE) have attracted a number of applications including optics, photonics, sensing, biosensing, filtration, seperations, microfluidics, catalysis, drug delivery, solar cells and nanofabrication[16, 19, 20].

Considerable research efforts have been focused to convert the diatom silica structures into technologically more suitable functional materials while preserving the frustule shapes and morphologies[19,21]. To convert biosilica into inorganic (MgO, TiO_2, zeolites), semiconducting (Si-Ge), metal (Au, Ag), carbon or organic (polyaniline) scaffolds, several approaches have been demonstrated including gas/solid displacement, chemical deposition, sol-gel synthesis and polymerization[20]. These studies have demonstrated that diatoms structure can be used as template for nanofabrication of metal, carbon and polymer nanostructures in combination with low-cost soft-lithographic approaches[20, 22]. Therefore, from these studies we come with idea to use diatoms as template or master mold to transform their complex morphologies into MnO_2 and address the problem of production

[a] *College of Material Science and Engineering, Chongqing University, Chongqing, 400044, P.R. China. E-mail: zhangyuxin@cqu.edu.cn*

[b] *School of Materials Science and Engineering, Ulsan National Institute of Science and Technology (UNIST), Ulsan 689-798, Republic of Korea*

[c] *National Key Laboratory of Fundamental Science of Micro/Nano-Devices and System Technology, Chongqing University, Chongqing, 400044, P.R. China*

[d] *School of Chemical Engineering*, The University of Adelaide, Adelaide, SA 5005, Australia. *E-mail: dusan.losic@adelaide.edu.au*

† Electronic Supplementary Information (ESI) available:EDS mapping. See DOI: 10.1039/b000000x/

3D electrodes for high-performance capacitors.

The aims of this work are two-fold: firstly to demonstrate the synthesis of a new MnO_2 based nanomaterials with uniqe 3-D morphology using diatoms as templates and secondly to demonstrate their application for high-performance capacitors. The idea is to explore supercapacitor properties of MnO_2 based on their 3-D structure and influence of shape at micron and nanoscale. Three types of hierarchical hollow MnO_2 patterns with both a large surface area and a 3D structure were successfully prepared by a template-assisted hydrothermal process. The schematic two-step formation process of the manganese oxide hollow structures with different morphologies is illustrated in Fig.1. The proposed process is based on hydrothermal reaction where in the first step $KMnO_4$ is used to obtain the nanostructured layer of MnO_2 on diatoms surface. In the second step diatom silica is removed and MnO_2 with diatom preserved shape and morphology is achived. The electrochemical and supercapacitors properties of prepared diatom/MnO_2 and MnO_2

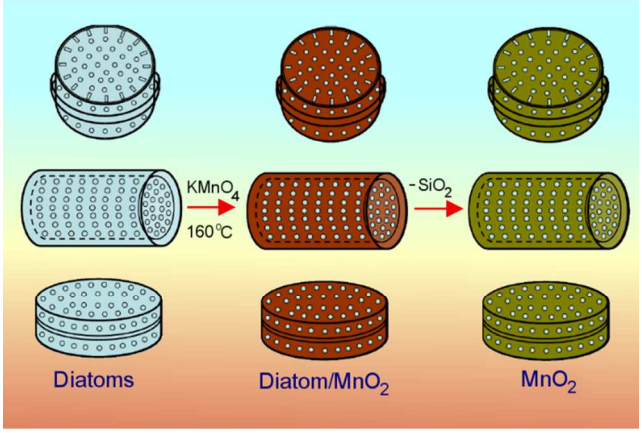

Figure 1. Schematic diagram showing the process of synthesis of diatom/MnO_2 and 3-D MnO_2 structures with replicated diatom's morphology.

replicas was performed, which exhibited ideal initial capacitive behavior and good cycling stability in a neutral electrolyte system.The presented fabrication process from diatom structure to MnO_2 replicas is environmentally friendly, low cost, and simple, which can be used for large scale production of supercapacitors materails and electrodes.

Experimental part

Materials and chemicals

Theew diatom species were employed in this study supplied from different sources: coscinodiscus-diatom (Tianjin Damao Chemical Reagent Company, PR China), melosira-diatom (Mount Sylvia Diatom Pty Ltd (Queensland, Australia), and navicula-diatom (The Culture Preservation Commission, Chinese Academy of Sciences, PR China). The first two are fossilised diatoms obtained from diatom mineral (DE) and third is cultured diatoms. All reagents were purchased from Alfa Aesar, and used without further processing. High-purity milli-Q water (18.2 MΩ) was used throughout the study.

Preparation of MnO_2 diatom replicas

Before the hydrothermal process, the diatoms were chemically treated by the following procedures. Typically, 5 g of materail was dispersed in 50 mL of deionized water with vigorous stirring. Afterwards, the sulfuric acid solution (50 g, 40 wt%) was dropwisely added into the mixture and the mixture was heat-treated at 100 ^oC for 4 h under constant magnetic stirring. Then 75 mL of deionized water was added, and the mixture was stirred for another 1 h. The acid-treated diatoms were separated by filtration and washed with deionized water to a pH value of about 7. Finally, the final products were heat-treated under mild temperature (450 ^oC) in a muffle stove to remove possible organic residues from diatom structures.

The MnO_2 replicas from diatoms were prepared using simple hydrothermal process without any surfactant. Briefly, purified diatom material (40~100 mg) was dispersed into the $KMnO_4$ solution (30 mL, 0.05 M) to form a homogeneous precursor. And then, the mixture was put into a Teflon-lined stainless steel autoclave which was subsequently maintained at 160 ^oC for 24 h. The obtained precipitate was collected by several rinse-centrifugation cycles and followed by immersing in a NaOH solution (5 mol L^{-1}) for 12 h to remove the diatom silica cores. The resulting product was collected by centrifugation, followed by washing with distilled water and finally dried in vacuum at 60 ^oC for 12 h, the amorphous manganese oxide hollow structures with different morphologies were obtained.

Characterization

The crystallographic information and chemical composition of as-prepared products were established by powder X-ray diffraction (XRD, Rigaku D/max 2500, Cu Kα). The morphological investigations of the purified diatoms and the MnO_2-modified diatom composites were carried out with focused ion beam (Zeiss Auriga FIB/SEM). Nitrogen adsorption-desorption isotherms were measured at 77 K with micrometritics ASAP 2020 sorptometer. The specific surface area was calculated with the Brunauer-Emmett-Teller (BET) equation, and the pore size distributions were calculated from the adsorption curve by the Barrett–Joyner–Halenda (BJH) method.

Electrochemical measurement

The electrochemical and supercapacitors properties of the prepared MnO_2 diatom replicas were carried out using an electrochemical workstation (CHI 660E) with three-electrode configuration in a 1 M Na_2SO_4 aqueous solution. The working electrode consisted of nickel foam as a current collector and a mixture of active materials, acetylene black and polyvinylidene difluoride (PVDF) with a weight ratio of 7:2:1. Platinum plate was used as the counter electrode and saturated calomel electrode (SCE) as the reference electrode, respectively. The positive electrodes were investigated by cyclic voltammetry (CV) technique in the potential range between -0.2 V and 0.8 V at various rates between 2-50 mV s^{-1}. Galvanostatic charge-discharge (CC) experiments were performed with current densities ranged from 0.25 to 10 A g^{-1} in the potential of -0.2 to 0.8 V. The electrochemical impedance spectroscopy (EIS) was conducted in the frequency range between 100 kHz and 0.01 Hz with a perturbation amplitude of 5 mV versus the open-circuit potential.

Results and discussion

Structural characterization of diatoms and their MnO_2 replicas

The morphology of the purified diatoms characterized by SEM is presented in Figs. 2a-c showing characteristic structures of three species *Coscinodiscus*, *Melosira* and *Navicula*,

respectively. The SEM images (Fig. 2 a1 and SI 1 a, b, c) show that coscinodiscus-diatom are disk-shaped with a diameter of 30–90 μm. The frustule possesses a highly developed nanoporous structure in which two types of macroporous structure are exhibited. The macropores in the center of shell arrays are not so regular and their pore sizes are concentrated at 300 nm–3 μm. The SEM images (Fig. 2 b1 and SI 1 d, e, f) show that melosira-diatom has perforated cylindrical shell and an opening at one end. Regularly spaced rows of pores of 300–500 nm diameters are located along the frustule shell wall. Particle size distribution measurement shows the size of diatom particles in the range of 10–20 μm. The SEM images (Fig. 2 c1 and SI 1 g, h, i) show that navicula-diatom shells are canoe-shaped and their width and length are 3–8 μm and 10–15 μm, respectively. Their nanoopores with diameters in the range of 100–200 nm are distributed on the frustule surface, which array in rows and are line-interlaced on each side of the frustule valve. However, most of the pores were not completely opened.

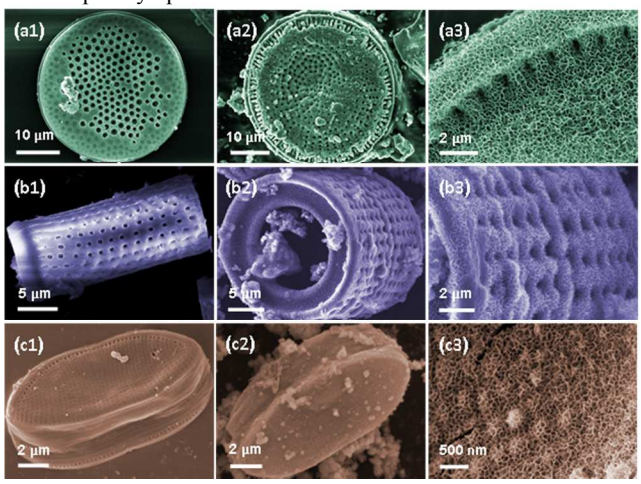

Figure 2. SEM images of diatom structures with different morphologies (left) and the corresponding diatom/MnO_2 core-shell structures (middle and right): Coscinodiscus-diatom (a1, a2, a3), Melosira-diatom (b1, b2, b3), and Navicula-diatom (c1, c2, c3), respectively.

Fig. 2 a2, b2 and c2 present the detailed morphologies of the as-prepared diatom@MnO_2 structures before removal of diatom template. The entire diatoms are decorated by MnO_2 nanosheets with smooth and uniform coating. It's worth noting from Figs. SI 2 a-c and d that the pores on the surface of coscinodiscus-diatom@MnO_2 and melosira-diatom@MnO_2 are still open with the uniform size diameter at about 300 and 250 nm , respectively, which would aid the diffusion of ions. In contrast, the pores on the surface of navicula-diatom @ MnO_2 are completely blocked (Fig. SI 2 e, f). Fig. 2 a3, b3 and c3 show the surface images of the diatom @ MnO_2, it can be seen that the MnO_2 nanosheets are well immobilized on the natural diatom, and the abundant ultrathin MnO_2 nanosheets are interconnected to each other, forming a highly porous surface morphology. The unique feature of the MnO_2 nanosheets could increase the specific surface area so as to make more electrical contact with the current collector, which may result in better charge transfer kinetics and an enhancive electrochemical capacity.

SEM images of hierarchical hollow MnO_2 patterns after removal of diatom templates are shown in Figs. 3 a-c. It can be seen that the obtained manganese oxide patterns almost maintain the corresponding morphology of the diatoms (Fig. 3 a1, b1 and c1). Compared with the three types of diatoms, two obvious characterizations can be observed for the obtained manganese oxide hollow architectures. Firstly, the manganese oxide hollow architectures well duplicate the size and shape of the diatom with differential morphologies after the SiO_2 core is etched in NaOH solution, and only some slight structural degradation such as collapse or amalgamation is observed during the etching process. Secondly, the rough shell thickness of the obtained manganese oxide hollow architectures is about 150-250 nm. In particular, more typical images (Fig. 3 a2, a3, b2, b3, c2 and c3) of the dehiscent MnO_2 patterns are also exhibited. It is obvious that the MnO_2 shell formed by interconnected ultrathin MnO_2 nanosheets still retain the replicated 3-D diatom morphology in spite of the disappearance of SiO_2 core.

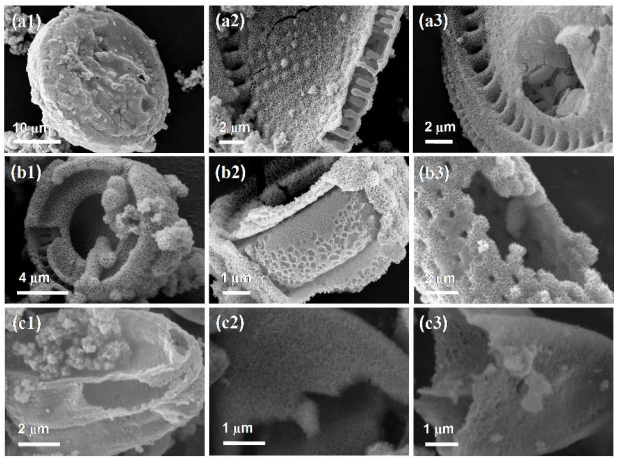

Figure 3. SEM images of the hierarchical hollow MnO_2 patterns by replica molding from diatom with different morphologies: Coscinodiscus-diatom (a1, a2, a3), Melosira-diatom (b1, b2, b3), and Navicula-diatom (c1, c2, c3), respectively.

Fig. 4 presents the composition and crystallite phase purity of the three types of diatom/MnO_2 core-shell structures. The diffraction peaks at 22.0 ° and 31.5 ° (Fig. 2a-c) could be assigned to the (101) and (102) planes of crystalline SiO_2 with the cristobalite structure[23, 24] (JCPDS card no. 39-1425, a = 4.973 Å, b = 4.973 Å, c =6.924 Å). The other diffraction peaks of 12.5 °, 25.2 °, 37.0 ° and 66.2 ° are in great accordance with the (001), (002), (-111) and (020) planes of birnessite-type manganese oxide

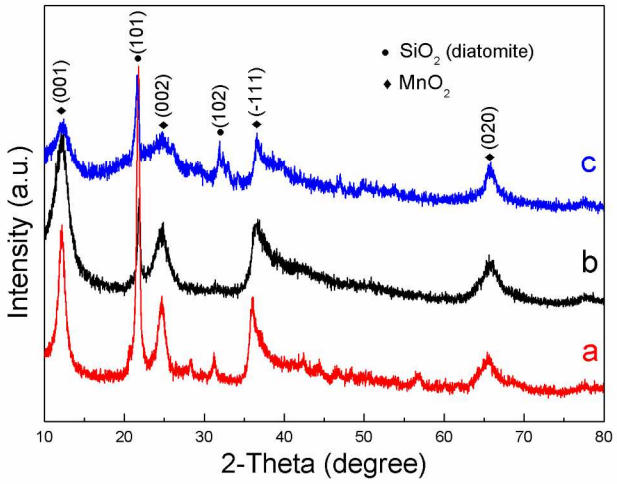

Figure. 4. XRD patterns of three types of diatom/MnO_2 core-shell structures obtained from three diatom species: (a) Coscinodiscus-diatom@MnO_2, (b) Melosira-diatom@MnO_2 and (c) Navicula-diatom@MnO_2, respectively.

crystal[25, 26] (JCPDS card no. 80-1098). The (101) diffraction peak in the XRD pattern of curve a is more intense than that of the other two curves, indicating that the percentages of SiO_2 content in coscinodiscus-diatom@MnO_2 is greater than that in melosira-diatom@MnO_2 and navicula-diatom@MnO_2, which might be caused by the large size of coscinodiscus-diatom (Fig. 2). In addition, the diffraction peak of MnO_2 in curve c is weaker than that of curve a and b, indicating an impaired crystallinity.

The XRD patterns of the hierarchical hollow MnO_2 structures obtained after removal of diatom silica template is presented in Fig. 5. Graphs were similar to each other showing a reflection characteristic of a typical birnessite-type manganese oxide, the diffraction peaks at about 12.5 °, 25.2 ° and 37.1 ° can be observed, corresponding to a basal spacing of 0.73 nm. These peaks are almost in accord with characteristic diffraction peaks of birnessite-type manganese

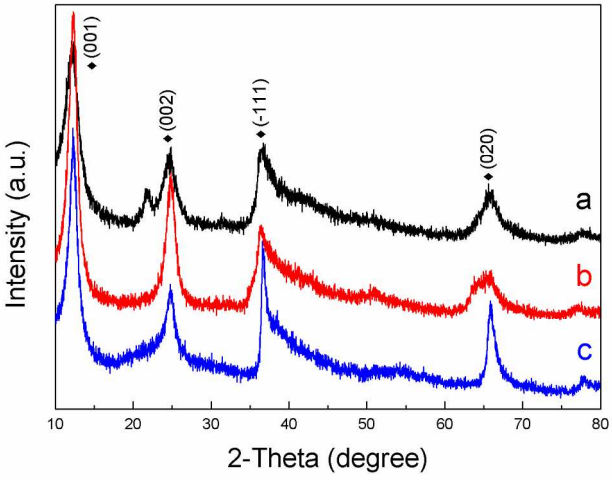

Figure. 5. XRD patterns of the hierarchical hollow MnO_2 replicas obtained from three diatom species after removal diatom tmplate: (a) MnO_2 Coscinodiscus replica, (b) MnO_2 Melosira replica, and (c) MnO_2 Navicula diatom replica. diatom

crystal (JCPDS card no. 80-1098). The diffraction peaks of SiO_2 in curve b and c had been completely disappeared. It implies that after etched in NaOH solution (5 mol/L), the SiO_2 cores of melosira-diatom@MnO_2 and navicula-diatom@MnO_2 are dissolved. In contrast, a very weak diffraction peak (indicated by a circle) at 22.0 ° which could be assigned to the (101) planes of cristobalite-type SiO_2 is observed in curve a, indicating a tiny residual of SiO_2 in coscinodiscus-type MnO_2 pattern. The scanning electron microscope (SEM) images and the corresponding energy dispersive X-ray spectrometry (EDS) elemental mapping of the MnO_2 structure show the uniform distribution of O, K and Mn elements (Fig. SI 3). Note that the signal for Si is not shown since the SiO_2 cores have been dissolved. The percentages of MnO2 in diatoms @ MnO2 is persnted in Table S1 (ESI)

The N_2 adsorption-desorption isotherms and the Barrett-Joyner-Halenda (BJH) pore size distribution curves (inset) of manganese oxide hollow structures with different morphologies are presented in Fig. 6 and Table S2 (ESI). It can be seen that all the isotherms of the three samples belong to type IV according to IUPAC classification[27, 28], indicating the presence of mesopores derived from the self-assembly of 2D nanosheet building blocks. The BET surface areas of the three samples show that the melosira-type MnO_2 pattern possesses the highest surface area ($67.3\ m^2\ g^{-1}$), while coscinodiscus-type MnO_2 pattern and navicula -type MnO_2 pattern have relative lower surface area (about $53.0\ m^2\ g^{-1}$ and $42.4\ m^2\ g^{-1}$). The BJH pore size distributions calculated from the desorption data indicate that the melosira-type MnO_2 pattern has a relative broad pore size distribution and the average pore diameter is about 12.4 nm. On the other hand, the average pore diameters of coscinodiscus-type MnO_2 pattern and navicula-type MnO_2 pattern are 15.5 nm and 14.0 nm, respectively. Such types of hierarchical surface morphologies with well-developed pore structures are advantageous for enhancive electro-chemical capacitors applications.

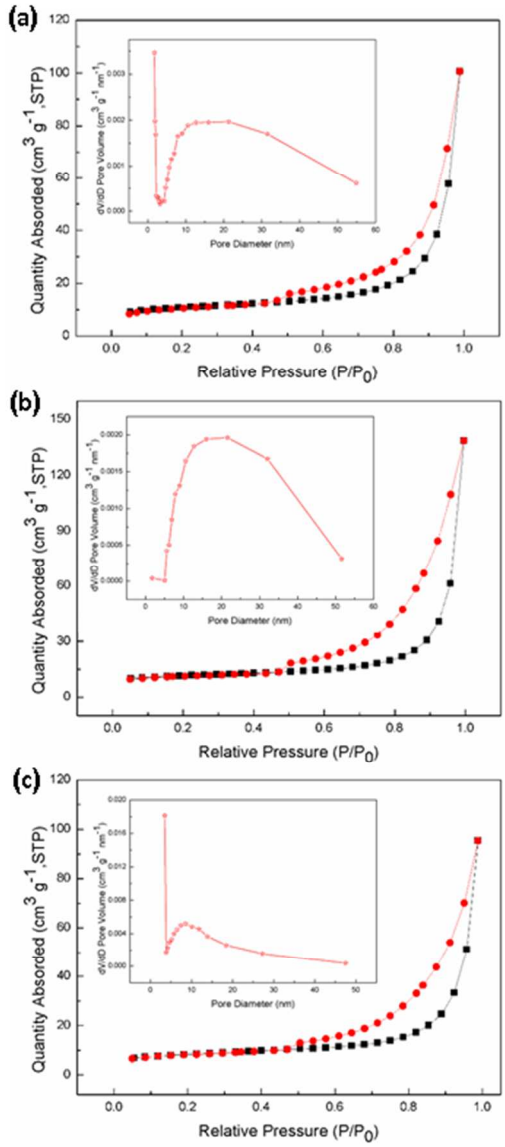

Figure. 6. Nitrogen adsorption-desorption isotherms of the hierarchical hollow MnO_2 patterns by replica molding from diatom with different morphologies: (a) Coscinodiscus-diatom, (b) Melosira-diatom, and (c) Navicula-diatom, respectively. The inset shows the corresponding BJH pore size distributions.

Electrechemical and supercapacitor characterization of Diatom/MnO_2 and MnO_2 diatom replicas

Cyclic voltammograms (CV) of the as-prepared diatom@MnO_2 structures are obtained in the three-electrode cell with 1 M Na_2SO_4 electrolyte. Fig. 7a shows CV curves at a scan

rate of 50 mV s^{-1}, in the potential window of −0.2 to 0.8 V. No obvious redox peaks are observed for the three electrodes, which are characteristic of electroactive MnO_2 in this range. The CV curves of coscinodiscus-diatom@MnO_2 and melosira-diatom@MnO_2 exhibited approximately rectangular shape with a slight distortion, indicating good capacitive behavior with rapid charge propagation. However, CV of the navicula-diatom@MnO_2 at the same rates is evidently more distorted with a smaller area. The reason might be responsible for the different capacitive performance: the denser packing of MnO_2 nanosheets which have completely blocked the pores on the surface navicula-diatom @ MnO_2 hindered effective transport of the electrolyte ions at higher scan rate.

The specific capacitance of the electrodes is calculated from the galvanostatic discharge curve using the following equation[29, 30]:

$$C_m = \frac{I\Delta t}{m\Delta V}$$

where m, I, Δt and ΔV are the weight (g) of the electroactive

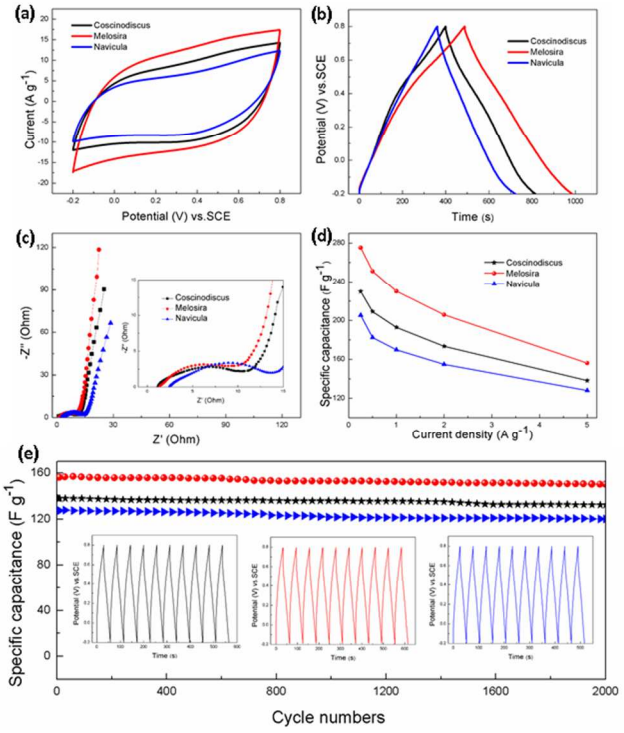

Figure 7. The electrochemical performance of the diatom/MnO_2 core-shell structures electrodes measured in 1 M Na_2SO_4 solution. (a) CV curves measured at a scan rate of 50 mV s^{-1}. (b) Galvanostatic charge/discharge curves at a current density of 0.5 A g^{-1}. (c) Electrochemical impedance spectrum at open circuit potential in the frequency range from 0.01 Hz to 100 kHz. (d) Specific capacitance under different current densities. (e) Cycling performance at the current density of 5 A g^{-1}. The inset shows the charge-discharge curves of the last 10 cycles.

materials, discharge current (A), the discharging time (s), and the discharging potential range (V), respectively. The specific capacitance of Coscinodiscus-diatom@MnO_2, Melosira-diatom@MnO_2 and Navicula-diatom@MnO_2 obtained from the discharging curves are calculated to be 209.2, 251.2 and 182.4 F g^{-1} at the current density of 0.5 A g^{-1}, respectively, as shown in Fig. 7b.

In order to further understand the electrochemical properties of diatom@MnO_2 electrodes, electrochemical impedance spectroscopy (EIS) analysis is carried out to provide information on electrochemical processes with different time constants. As shown in Fig. 7c, the three Nyquist plots are similar to each other with a depressed semicircle in the high-to-medium frequency region arising from the chemical reaction process and a straight line in the low-frequency region which is corresponding to ion diffusion in the electrode material. The measured impedance spectra can be fitted by using Zsimpwin on the basis of the equivalent circuit consisting of Rs, a combination of the contact resistance of the active materials with substrate and the test cell to the apparatus, the ionic resistance of electrolyte, the intrinsic resistance of electrodes, a charge-transfer resistance (Rct), a double-layer capacitance (CPE), and Warburg impedance (Zw). The Rct values (the inset plot magnified of Fig. 4c) of coscinodiscus-diatom @ MnO_2, melosira-diatom @ MnO_2 and navicula-diatom@MnO_2 are about 8.8, 7.5 and 11.3 Ù, and the Rs values are about 1.22, 1.25 and 2.5Ù , respectively. Graphs from Fig. 7d confirmed that the capacitances of the diatom@MnO_2 structures decrease slightly with increasing current density from 0.25 to 5 A g^{-1}. Coscinodiscus-diatom@MnO_2, melosira-diatom@MnO_2 and navicula-diatom@MnO_2 electrodes display good high rate performance with 60.15 %, 56.74 % and 62.34 % of their initial capacitance being maintained when the current density increases to 5 A g^{-1}, respectively.

The diatom@MnO_2 electrodes are subjected to an extended charge-discharge cycling at 5 A g^{-1} and the result is depicted in Fig. 7e. After 2000 cycles, 95.9 %, 96.2 % and 94.1 % of the original capacitance is reserved for coscinodiscus-diatom@MnO_2, melosira-diatom@MnO_2 and navicula-diatom@MnO_2 electrodes, respectively, indicating the porous diatom@MnO_2 structures have good cycle stability. In addition, the charge-discharge curves of the last 10 cycles of 2000 cycles are shown as the inset in Fig. 7e. It can be seen that the curves revealed a highly linear and symmetric shape with small resistance drops, further confirming the excellent supercapacitive behavior and superior electrochemical reversibility.

The pseudocapacitive behavior of the manganese oxide hollow structures in three electrode configuration are also investigated (Fig. 8). The CV profile (Fig. 8a) of the MnO_2 hollow replica structures deviates from rectangularity and transform into spindle shape compared with the corresponding diatom@ MnO_2 structures. This can be ascribed to poor electrical conductivity and some collapse or amalgamation of the change of ion transplant surrounding, for which the ions can only reach the outer surface of the MnO_2 hollow structures electrode. The specific capacitance of coscinodiscus-type MnO_2 pattern, melosira-type MnO_2 pattern and navicula-type MnO_2 pattern obtained from the discharging curves are calculated to be 301.2, 371.2 and 237.3 F g^{-1} at the current density of 0.5 A g^{-1}, respectively, as shown in Fig. 8b. From the EIS analysis (Fig. 8c), the Rct values of coscinodiscus-type MnO_2 pattern, melosira-type MnO_2 pattern and navicula-type MnO_2 pattern are about 5.8, 4.1 and 6.3 Ù, and the Rs values are about 1.21, 1.26 and 3.2 Ù, respectively. The rate performance with 51.9 %, 54.7% and 51.8 % of their initial capacitance being maintained are obtained when the current density increases from 0.5 to 10 A g^{-1}, respectively. A comparison of the specific capacitance of the diatoms @ MnO2 from our work and MnO2 nanostructures presented in previous reports showing superior performance of this material (Table S3, ESI).

Finaly, the prepared MnO_2 diatom replica electrodes are subjected to an extended charge-discharge cycling at 5 A g^{-1} and the result is depicted in Fig. 8e. After 2000 cycles, 92.5 93.9 % and 90.6 % of the original capacitance is reserved for coscinodiscus-type MnO_2 pattern, melosira-type MnO_2 pattern

and navicula-type MnO_2 pattern electrodes, respectively. In addition, the charge-discharge curves of the last 10 cycles of 2000 cycles are also shown as the inset in Fig. 8e, the charge curves are still symmetric as compared to their corresponding discharge counterparts, indicating no significant structural change for the electrodes during the charge-discharge processes.

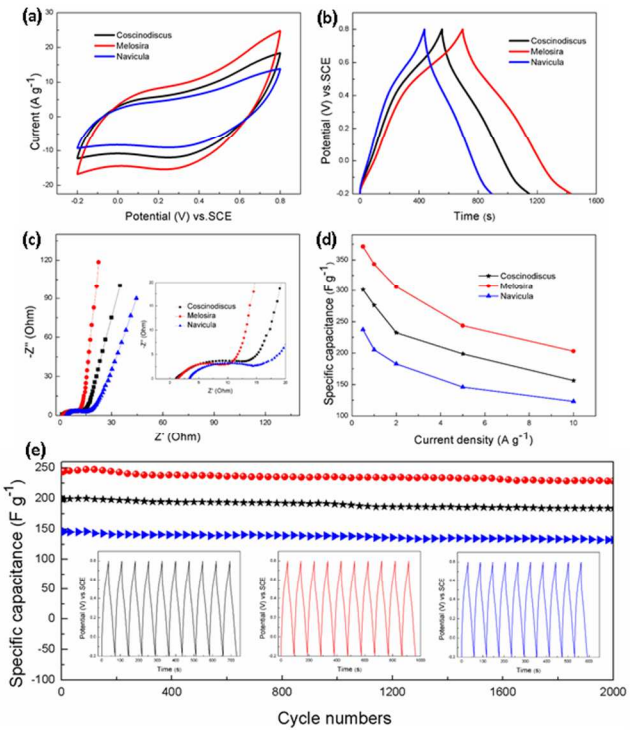

Figure. 8. The electrochemical performance of the hierarchical hollow MnO_2 patterns electrodes measured in 1 M Na_2SO_4 solution. (a) CV curves measured at a scan rate of 50 mV s^{-1}. (b) Galvanostatic charge/discharge curves at a current density of 0.5 A g^{-1}. (c) Electrochemical impedance spectrum at open circuit potential in the frequency range from 0.01 Hz to 100 kHz. (d) Specific capacitance under different current densities. (e) Cycling performance at the current density of 5 A g^{-1}. The inset shows the charge-discharge curves of the last 10 cycles.

Conclusions

In summary, we have reported for the first time the successful synthesis of tree types of 3-D diatom/MnO_2 and MnO_2 replica structures with unique diatom morphologies prepared using diatoms as templates. SEM, XRD and BET analysis confirmed that prepared MnO_2 structures have preserved diatom shape, 3-D morphology, with micro and nano features and porosity. The electrochemical characterization of the MnO_2 diatom replicas used as the electrode for supercapacitor showed an excellent performance with high specific capacitance; good cyclability and rate capability. It was found that these performances are dependent of the shape and the best results are obtained from MnO_2 electrodes with melosira diatom replica. This work demonstrated that diatom can be used as template for nanofabrication of 3-D metal nanostructures with complex 3-D architectures and use for high-performance capacitors. Th presented synthetic approach is generic, scalable, and in combination with low-cost soft-lithographic approaches can be used for low-cost device production.

Acknowledgments

The authors gratefully acknowledge the financial supports provided by National Natural Science Foundation of China (Grant no. 51104194), National Key laboratory of Fundamental Science of Micro/Nano-device and System Technology (2013MS06, Chongqing University), State Education Ministry and Fundamental Research Funds for the Central Universities (Project no. CDJZR12248801, CDJZR14135501, and CDJZR13130035, Chongqing University, PR China) and the Australian Research Council (FT 110100711), the Grain Research and Development Corporation (GRDC) and Mount Sylvia pty.ltd.

References

1 L.L.Peng, X.Peng, B.R.Liu, C.Z.Wu, Y.Xie and G.H.Yu, Nano Lett., 2013, 13, 2151-2157.
2 J.Y.Tao, N.S.Liu, L.Y.Li, J.Su and Y.H.Gao, Nanoscale, 2014, 6, 2922-2928.
3 W.F.Wei, X.W.Cui, W.X.Chen and D.G.Ivey, Chem. Soc. Rev., 2011, 40, 1697-1721.
4 K.Kai, Y.Kobayashi, Y.Yamada, K.Miyazaki, T.Abe, Y.Uchimoto and H. Kageyama, J. Mater. Chem., 2012, 22, 14691-14695.
5 M.X.Liu, L.H.Gan, W.Xiong, Z.J.Xu, D.Z.Zhu and L.W.Chen, J. Ma ter. Chem. A, 2014, 2, 2555–2562.
6 M.Su, Y.Zhang, X.R.Song, S.G.Ge, M.Yan, J.H.Yu and J.D. Huang, Electrochim. Acta, 2013, 97, 333-340.
7 P.H.Yang, Y.Ding, Z.Y.Lin, Z.W.Chen, Y.Z.Li, P.F.Qiang, M.Ebrahimi, W.J.Mai, C.P.Wong and Z.L.Wang, Nano Lett., 2014, 14, 731-736.
8 P.H.Yang, Y.Z.Li, Z.Y.Lin, Y.Ding, S.Yue, C.H.Wong, X.Cai, S.Z.Tan and W.J.Mai, J. Mat er. Chem. A, 2014, 2,595–599.
9 S.Park, I.Nam, G.P.Kim, J.W.Han and J.Yi, ACS Appl. Mater. Interfaces, 2013, 5, 9908-9912.
10 Q.Li, Z.L.Wang, G.R.Li, R.Guo, L.X.Ding and Y.X.Tong, Nano Lett., 2012, 12, 3803-3807.
11 Y.Gu, J.W.Cai, M.Z.He, L.P.Kang, Z.B.Lei and Z.H.Liu, J. Power Sources, 2013, 239, 347-355.
12 X.H.Tang, Z.H.Liu, C.X.Zhang, Z.P.Yang and Z.L.Wang, J. Power Sources, 2009, 193, 939-943.
13 M.Huang, Y.X.Zhang, F.Li, L.L.Zhang, R.S.Ruoff, Z.Y.Wen and Q.Liu, Sci. Rep., 2014, 4, 3878.
14 H.J.Zheng, J.X.Wang, Y.Jia and C.A.Ma, J. Power Sources, 2012, 216, 508-514.
15 D.Liu, W.W.Yuan, P.Yuan, W.B.Yu, D.Y.Tan, H.M.Liu, H.P.He, Appl. Surf. Sci., 2013, 282, 838-843.
16 D.Losic, G.Triani, P.J.Evans, A.Atanacio, J.G.Mitchell and N.H.Voelcker, J. Mater. Chem., 2006, 16, 4029-4034.
17 Y.X.Zhang, X.D.Hao, F.Li, Z.P.Diao, Z.Y.Guo and J.Li, Ind. Eng. Chem. Res., 2014, 53, 6966-6977.
18 C.Jeffryes, J.Campbell, H.Li, J.Jiao and G.Rorrer, Energy Environ. Sci., 2011, 4, 3930-3941.
19 D.Losic, Y.Yu, M.S.Aw, S.Simovic, B.Thierry and J.Addai-Mensah, Chem. Commun., 2010, 46, 6323-6325.
20 D.Losic, J.G.Mitchell, R.Lal and N.H.Voelcker, Adv. Funct. Mater., 2007, 17, 2439-2446.
21 M.S.Wang, L.Z.Fan, M.Huang, J.H.Li and X.H.Qu, J. Power Sources, 2012, 219, 29-35.
22 D.Losic, J.G.Mitchell and N.H.Voelcker, Chem. Commun., 2005, 4905-4907.
23 Y.X.Zhang, M.Huang, F.Li, X.L.Wang and Z.Q.Wen, J. Power Sources, 2014, 246, 449-456.
24 K.D.Xia, C.X.Lu and Y.Yang, Appl. Surf. Sci. 2013, 265, 603-609.
25 L.Yu, G.Q.Zhang, C.Z.Yuan and X.X.Lou, Chem. Commun., 2013, 49, 137-139.

26 Y.J.Huang, Y.L.Lin and W.S.Li, Electrochim. Acta, 2013, 99, 161-165.
27 M Kruk and M Jaroniec, Chem. Mater., 2001, 13, 3169-3183.
28 G.Y.Gor, M.Thommes, K.A.Cychosz and A.V.Neimark, Carbon. 2012, 50, 1583-1590.
29 S.J.Ding, T.Zhu, J.S.Chen, Z.Y.Wang, C.L.Yuan and X.W.Lou, J. Mater. Chem., 2011, 21, 6602-6606.
30 J.Y.Liao, D.Higgins, G.Lui, V.Chabot, X.C.Xiao and Z.W.Chen, Nano Lett., 2013, 13, 5467-5473.

Graphical abstract

The synthesis of MnO_2 with uniqe and complex 3-d morphology replicated from diatoms and their outstanding electrochemical properties for high-performance supercapacitors are demonstarted